

Negative Capacitance in Multidomain Ferroelectric Superlattices

Authors: Pavlo Zubko^{1*}, Jacek C. Wojdeł^{2*}, Marios Hadjimichael¹, Stéphanie Fernandez-Pena³, Anaïs Sené⁴, Igor Luk'yanchuk^{4,5}, Jean-Marc Triscone³, Jorge Íñiguez^{6,2}

Affiliations:

¹London Centre for Nanotechnology and Department of Physics and Astronomy, University College London, 17-19 Gordon Street, London WC1H 0HA, United Kingdom.

² Institut de Ciència de Materials de Barcelona (ICMAB-CSIC), Campus UAB, 08193 Bellaterra, Spain.

³Department of Quantum Matter Physics, University of Geneva, CH-1211 Geneva, Switzerland.

⁴Laboratory of Condensed Matter Physics, University of Picardie, Amiens, 80000, France.

⁵L. D. Landau Institute for Theoretical Physics, Moscow, Russia.

⁶Materials Research and Technology Department, Luxembourg Institute of Science and Technology (LIST), 5 avenue des Hauts-Fourneaux, L-4362 Esch/Alzette, Luxembourg.

*These authors contributed equally to this work.

The stability of the spontaneous electrical polarisation characteristic of ferroelectrics is fundamental to a multitude of their current applications, ranging from the simple electrical cigarette lighter to non-volatile random access memories¹. Yet, the technological potential of these materials is far from being exhausted as research on nanoscale ferroelectrics reveals their properties to be profoundly different from those in bulk, giving rise to fascinating new phenomena with exciting prospects for future

devices²⁻⁴. As ferroelectrics become thinner, maintaining a stable polarisation becomes increasingly challenging. On the other hand, intentionally destabilising this polarisation can cause the effective electrical permittivity of a ferroelectric to become negative⁵, enabling it to behave as a negative capacitance when integrated in a heterostructure. Negative capacitance has been garnering increasing attention following the realisation that it could be exploited to overcome fundamental limitations on the power consumption of field effect transistors⁶. Experimentally, however, demonstrations of this phenomenon are still contentious⁷. The prevalent interpretations based on homogeneous polarisation models are difficult to reconcile with the expected strong tendency for domain formation^{8,9}, while the effect of domains on negative capacitance has received surprisingly little attention^{5,10-12}. Here we report the observation of negative capacitance in a model system of *multidomain* ferroelectric-dielectric superlattices across a wide range of temperatures, in both the ferroelectric and paraelectric phases. Using a phenomenological model we show that domain-wall motion not only gives rise to negative permittivity but can also enhance, rather than limit, its temperature range. Furthermore, our first-principles-based atomistic simulations provide detailed microscopic insight on the origin of this phenomenon, identifying the dominant contribution of near-interface layers and paving the way for its future exploitation.

Negative capacitance (NC) has its origins in the imperfect screening of the spontaneous polarisation^{5,10,13,14}. Imperfect screening is intrinsic to any semiconductor-ferroelectric or even metal-ferroelectric interfaces because of their finite effective screening lengths^{15,16}. Alternatively, it can be engineered in a controlled manner by deliberately inserting a dielectric layer of relative permittivity ϵ_d between the ferroelectric and the electrodes as suggested by Salahuddin and Data⁶ and shown in Fig. 1a. The physical separation of the

ferroelectric bound charge from the metallic screening charges creates a depolarizing field inside the ferroelectric, destabilizing the polarisation and lowering the ferroelectric transition temperature. The effect of the dielectric layer can be understood by considering the free energy of the bilayer capacitor with the usual assumption of a uniform polarisation P (see Methods). Below the bulk transition temperature T_0 , the free energy of the ferroelectric layer develops a double-well with minima at finite values of P , but when combined with the parabolic potential of the dielectric layer the total energy has a minimum at $P = 0$ (Fig. 1b). The reciprocal dielectric constant of the system as a whole ϵ^{-1} , given by the curvature of the total energy with respect to the polarisation, is positive, as required for thermodynamic stability. However, as the non-polar state of the ferroelectric layer corresponds to a maximum of *its local* energy, the *local* stiffness of the ferroelectric layer is negative, i.e., polarising the ferroelectric layer has a negative energy cost.

With decreasing temperature, the ferroelectric double-well progressively deepens and would dominate the total energy below $T = T_C^h$, favouring a transition to a homogeneous ferroelectric state. The local dielectric stiffness of the ferroelectric layer would then increase and eventually become positive as shown by the blue curve in Fig. 1c. This ‘homogeneous’ model has served as the basis for the interpretation of the experimental studies of NC to date¹⁷⁻²⁰. However, despite its attractive simplicity, it does not describe the true ground state of the system as, in general, the depolarization field that leads to the NC effect will also tend to favour instead a transition to an inhomogeneous, multidomain phase at $T_C^{ih} > T_C^h$ as demonstrated by numerous experiments (e.g., ref. 8). This has profound consequences for the dielectric response and NC, as we show next with the help of two phenomenological models. First, we use a Ginzburg-Landau approach, as detailed in Methods, to obtain an analytic description of the phase transition into an inhomogeneous state with a gradual (soft) polarization profile, typical of ultrathin films²¹. This model allows us to obtain the lattice

contribution to the dielectric response (i.e. the response of a static domain structure), which is shown by the dashed curve in Fig. 1c. The appearance of the soft domain structure results in qualitative changes in the shape of the $\epsilon^{-1}(T)$ curve, pushing its minimum below the actual transition temperature. The overall effect of a static domain structure, however, is to reduce the temperature range of NC, as previously thought¹¹.

To investigate the contribution of domain wall motion, we choose instead to work in the simpler Kittel approximation, which is valid for abrupt (thin) domain walls typical of thicker films well below T_C ^{5,12,22}. The resulting dielectric response is shown by the solid red curve in Fig. 1c (for details of the calculation, see Methods). Remarkably, domain wall motion contributes negatively to the overall dielectric stiffness^{5,10,12}: Macroscopically, domain wall displacements create a net polarisation that leads to a depolarising field, which dominates the total field in the ferroelectric, thus leading to NC. Microscopically, the domain wall displacements redistribute the interfacial stray fields resulting in a negative net contribution to the free energy and thus the local dielectric constant. Although the thin-wall Kittel model does not capture the subtleties of the soft domain structure of ultrathin films, it clearly highlights the importance of the domain wall contribution in extending the temperature window of the NC effect.

To experimentally access the different temperature regimes of NC shown in Fig. 1c, we have deposited several series of high-quality epitaxial superlattices consisting of n_f ferroelectric and n_d dielectric monolayers repeated N times, and hereafter labelled $(n_f, n_d)_N$. For each superlattice series n_f is fixed, while n_d is varied from 4 to 10 unit cells. SrTiO₃ (STO) crystals were used as substrates and epitaxial SrRuO₃ (SRO) top and bottom electrodes were deposited *in-situ* to enable dielectric impedance spectroscopy measurements. STO was also chosen as the dielectric component, while PbTiO₃ (PTO) and quasi-random Pb_{0.5}Sr_{0.5}TiO₃

(PST) alloys were used as the ferroelectric layers. The PST composition was chosen for its low T_0 , enabling us to investigate the full range of temperatures up to and above T_0 without complications arising from leakage.

Such superlattices constitute a model system for the observation of NC, as they are mathematically equivalent to the bilayer systems investigated theoretically^{5,6,21} and present a number of very convenient features – e.g., the small layer thicknesses minimize the number of free carriers, ensuring appropriate electrostatic boundary conditions, while the highly ordered stripe domains are well-suited for X-ray diffraction studies and theoretical modelling. Crucially, by varying the dielectric layer thicknesses and the total number of bilayer repetitions, the individual layer permittivities can be extracted from measurements of the total capacitance of a series of samples as we show next.

The dielectric properties of three PST- STO superlattices with 14-uc-thick PST layers are summarized in Fig. 2a-d. All superlattices exhibit a broad maximum in the dielectric response which moves to lower temperature with increasing STO content (Fig. 2a). These maxima do not coincide with the phase transition temperature T_C^{ih} and instead arise from the qualitatively different temperature dependences of the STO and PST layer permittivities. Using XRD, we obtain an estimate of T_C^{ih} from the temperature evolution of in-plane and out-of-plane lattice parameters (a and c , respectively) as shown in Fig. 2b. Contrary to what is expected for a transition to a homogeneous ferroelectric state, the observed T_C^{ih} is independent of the STO layer thickness as T_C^{ih} is determined by the domain wall density, which in turn depends only on the ferroelectric layer thickness. The regular domain structure with a periodicity of ~10–12 nm can be observed using XRD as peaks in the diffuse scattering around the superlattice Bragg reflections (Extended Data Fig. 1).

To separate the individual layer dielectric constants ϵ_d and ϵ_f we apply the standard series capacitor expression, which for our superlattices can be written as $\frac{n}{\epsilon} \approx \frac{n_d}{\epsilon_d} + \frac{n_f}{\epsilon_f}$ (see Methods), where $n = n_d + n_f$ and ϵ is the overall dielectric constant of the superlattice, obtained directly from the measured capacitance. The linear relationship between n/ϵ and n_d is well satisfied for $100 \text{ K} \lesssim T < 570 \text{ K}$, as illustrated in Fig. 2c for a few selected temperatures. The dielectric constant of the STO layers can be obtained from the slopes of the plots in Fig. 2c. The resulting $\epsilon_d(T)$ is presented in the inset of Fig. 2d and shows the typical decrease with temperature observed in STO thin films and bulk crystals. The intercepts of the linear plots in Fig. 2c give the reciprocal dielectric constant of the PST layers ϵ_f^{-1} , which is plotted in Fig. 2d. At low temperature, deep in the ferroelectric regime, ϵ_f^{-1} is positive. Upon heating, however, it slowly decreases entering the NC regime around room temperature. It then reaches a minimum, and subsequently returns to positive values at high temperature in the paraelectric phase. Note that the minimum in ϵ_f^{-1} is observed well below the phase transition temperature T_C (indicated with an arrow), contrary to what would be expected for a structure with a homogeneous polarisation. For this series of samples, the temperature regime $T_C^{ih} < T < T_0$ cannot be resolved because T_C^{ih} is very close to T_0 (measured independently to be around 500 K for PST thin films of the same composition). In order to access this temperature regime, a set of $(5, n_d)_N$ superlattices was fabricated with PST replaced by PTO, which has a much higher T_0 ($\sim 1200 \text{ K}$) when grown coherently on SrTiO_3 ²³. As shown in Fig. 2e, the NC regime can be clearly observed in the paraelectric phase above $T_C^{ih} \approx 580 \text{ K}$ in these samples. Above T_C , however, the dielectric stiffness increases much faster than expected, turning positive far below T_0 . This is most likely due to the progressive increase in the thermally activated conductivity of the ferroelectric layers, which destroys the

electrostatic boundary conditions required for NC and leads to Maxwell-Wagner relaxations at high temperature (see Methods).

To gain further insight, we used first-principles-based effective models that permit treating thermal effects. We used the potentials for PTO and STO introduced in ref. 24 as the starting point to construct models for PTO/STO superlattices with an in-plane epitaxial constraint corresponding to a STO-(001) substrate (see Methods). As compared with experiment, our models feature relatively stiff STO layers and relatively low ferroelectric transition temperatures; otherwise they capture the behaviour of PTO layers stacked with dielectric layers in a qualitatively and semi-quantitatively correct way. For computational feasibility, we focused on a representative (8,2) superlattice (10x10x10 elemental perovskite cells in the periodically-repeated simulation box) that presents the behaviour summarized in Fig. 3. As we cool down from high temperature, the c/a ratio of the PTO layers (Fig. 3a) marks an elastic transition, at about 490 K, to a state characterized by strongly fluctuating ferroelectric domains (380 K snapshot in Fig. 3d and Supplementary Video). This fluctuating phase could be indicative of temperature-induced domain melting, analogous to vortex lattice melting in high- T_C superconductors²⁵. As we further cool down, we observe a ferroelectric transition at 370 K associated with the freezing of the domains into stable stripes. This change can be appreciated in Fig. 3b, where we plot different measures of the local dipole order inside the PTO layer. As shown in the bottom panel of Fig. 3d, this low-temperature phase presents stripes along the [110] direction, with a domain thickness of about 5 unit cells and sharp walls. As shown in Fig. 3f and Extended Data Fig. 2, in the ground state the dipoles form closure domains and almost do not penetrate inside the stiff STO layers. This corresponds to the vanishing of spontaneous polarization at the surface of a polydomain ferroelectric noted in ref. 26. Note that the domain walls present a significant Bloch character in the ground

state; this is the result of a wall-confined polarization along [-110] that appears at about 120 K and is analogous to the one recently predicted for pure PTO²⁷.

We investigated the layer-resolved dielectric response of the superlattices. In essence (more details in Methods), we compute the local susceptibility of a region i , $\chi_i = \frac{1}{\epsilon_0} \frac{\partial \langle P_i \rangle}{\partial E_{ext}}$, where P_i is the local polarization and $\langle \dots \rangle$ represents a thermal average that can be readily obtained by simulating our models under an applied electric field E_{ext} . As shown in Methods, the local dielectric constant can be expressed as $\epsilon_i = \frac{\epsilon_{tot}}{\epsilon_{tot} - \chi_i}$, where ϵ_{tot} is the dielectric constant of the whole system. The results in Fig. 3c correspond to such a calculation for the PTO layers of the (8,2) superlattice and confirm the presence of a NC region extending above and below the ferroelectric transition temperature.

So where does the computed NC come from? The local susceptibilities χ_i are always positive in our calculations, confirming the expectation that an applied external field induces polarisation changes that are parallel to it. By contrast, the local dielectric constant ϵ_i measures a response to a local field incorporating depolarising fields that make its behaviour richer and its physical interpretation more challenging⁵. In particular, its value will be negative if $\chi_i > \epsilon_{tot}$. Hence, the NC regions are those significantly more responsive than the system as a whole.

Our formalism allows us to map out the local response within the PTO layers and thus determine which regions are responsible for the NC behaviour. Figure 3e shows ϵ_i^{-1} resolved along the superlattice-stacking direction and as a function of temperature. At high temperatures the material behaves like a normal dielectric. Then, negative contributions to ϵ_f^{-1} appear at about 550 K, well before any ordering occurs in the system; in that regime, the negative contribution is confined to the vicinity of the PTO/STO interface, and the response of the whole PTO layer continues to be positive. As temperature is further reduced, the NC

region extends to the whole PTO layer. Eventually, at low temperature, the inner part of the PTO layer recovers a conventional dielectric behaviour that dominates the total response, even if our simulations reveal that a negative contribution from the interfaces still persists.

We can further map the susceptibility within the planes perpendicular to the stacking direction to thus quantify the contributions of domains and domain walls. Figure 3f shows representative results at 320 K. Predictably, we find that the susceptibility at the domain walls is much larger than at the domains. In other words, the field-induced polarization of the walls, which results in the growth/shrinkage of the domains, dominates the response. Further, the large response of the walls is much enhanced in the vicinity of the interfaces with the STO layers. Hence, our simulations suggest that, below ~ 370 K, the domain wall region near the interfaces dominates the NC of the PTO layers.

There are important differences between our simulated and experimental superlattices, which complicates a detailed comparison (more in Methods). Nevertheless, our basic result, i.e. that the PTO layers present a negative dielectric constant in a temperature region extending above and below T_C , is confirmed by our simulations. Further, we also ran simulations of various (8,m) superlattices to mimic our experimental approach to compute the response of the PTO layer; the results shown in Extended Data Fig. 3 are similar to those of Fig. 3c, thus validating our strategy to measure ϵ_f .

Finally, as mentioned at the outset, the depolarisation effects in ferroelectric-dielectric superlattices are completely analogous to those at interfaces between a ferroelectric and a metal or a semiconductor. We have found that PTO-SRO superlattices, for example, exhibit very similar domain structures as PTO-STO. These are induced by the imperfect screening at the SRO-PTO interfaces, which produces a depolarizing field equivalent to that induced by a 7 u.c.-thick STO layer^{28,29}. It is therefore reasonable to expect the same order of magnitude NC effect in a transistor-like structure composed of a PTO gate dielectric and an ultrathin

conducting SRO channel, where applying a gate voltage V_g will lead to an enhancement of the surface potential ϕ_s at the PTO-SRO interface. With a PTO-SRO interface capacitance of $\sim 0.6 \text{ F/m}^2$ ¹⁴ and a ferroelectric capacitance C_f equivalent to that of one of our PTO layers, one can obtain voltage amplification factors $\frac{\partial \phi_s}{\partial V_g} = \frac{C_f}{C_i + C_f}$ as large as ~ 2 at temperatures where $1/\epsilon_f$ is most negative. For the more practical interface with a conventional semiconductor, the expected amplification is more modest (e.g., $\frac{\partial \phi_s}{\partial V_g} \sim 1.03$ for $C_i \sim 0.1 \text{ F/m}^2$ ¹¹) but is still enhanced over conventional gate dielectrics where the corresponding value is below unity. Such enhancements are especially encouraging in the light of tremendous recent progress in the integration of ferroelectric oxides directly on conventional semiconductors³⁰.

References

- 1 Scott, J. F. & Paz de Araujo, C. A. Ferroelectric Memories. *Science* 246, 1400-1405, (1989).
- 2 Naumov, I. I., Bellaiche, L. & Fu, H. Unusual phase transitions in ferroelectric nanodisks and nanorods. *Nature* 432, 737-740, (2004).
- 3 Garcia, V. *et al.* Giant tunnel electroresistance for non-destructive readout of ferroelectric states. *Nature* 460, 81-84, (2009).
- 4 Kim, D. J. *et al.* Ferroelectric Tunnel Memristor. *Nano Lett* 12, 5697-5702, (2012).
- 5 Bratkovsky, A. M. & Levanyuk, A. P. Very large dielectric response of thin ferroelectric films with the dead layers. *Phys Rev B* 63, 132103 (2001).
- 6 Salahuddin, S. & Datta, S. Use of negative capacitance to provide voltage amplification for low power nanoscale devices. *Nano Lett* 8, 405-410, (2008).
- 7 Krowne, C. M., Kirchoefer, S. W., Chang, W., Pond, J. M. & Alldredge, L. M. B. Examination of the Possibility of Negative Capacitance Using Ferroelectric Materials in Solid State Electronic Devices. *Nano Lett* 11, 988-992, (2011).
- 8 Fong, D. D. *et al.* Ferroelectricity in ultrathin perovskite films. *Science* 304, 1650-1653, (2004).
- 9 Catalan, G., Jimenez, D. & Gruverman, A. FERROELECTRICS Negative capacitance detected. *Nat Mater* 14, 137-139, (2015).
- 10 Bratkovsky, A. M. & Levanyuk, A. P. Depolarizing field and "real" hysteresis loops in nanometer-scale ferroelectric films. *Appl Phys Lett* 89, 253108 (2006).
- 11 Cano, A. & Jimenez, D. Multidomain ferroelectricity as a limiting factor for voltage amplification in ferroelectric field-effect transistors. *Appl Phys Lett* 97, 133509-, 133509 (2010).
- 12 Luk'yanchuk, I. P., A.; Sidorkin, A.; Vinokur, V. Terahertz Electrodynamics of 180° Domain Walls in Thin Ferroelectric Films. *arXiv:1410.3124* (2014).
- 13 Ponomareva, I., Bellaiche, L. & Resta, R. Dielectric anomalies in ferroelectric nanostructures. *Phys Rev Lett* 99, 227601 (2007).
- 14 Stengel, M., Vanderbilt, D. & Spaldin, N. A. Enhancement of ferroelectricity at metal-oxide interfaces. *Nat Mater* 8, 392-397 (2009).
- 15 Mehta, R. R., Silverman, B. D. & Jacobs, J. T. Depolarization Fields in Thin Ferroelectric Films. *J Appl Phys* 44, 3379-3385 (1973).
- 16 Junquera, J. & Ghosez, P. Critical thickness for ferroelectricity in perovskite ultrathin films. *Nature* 422, 506-509 (2003).

- 17 Khan, A. I. *et al.* Experimental evidence of ferroelectric negative capacitance in nanoscale heterostructures. *Appl Phys Lett* **99**, 113501 (2011).
- 18 Appleby, D. J. R. *et al.* Experimental Observation of Negative Capacitance in Ferroelectrics at Room Temperature. *Nano Lett* **14**, 3864-3868 (2014).
- 19 Gao, W. *et al.* Room-Temperature Negative Capacitance in a Ferroelectric–Dielectric Superlattice Heterostructure. *Nano Lett* **14**, 5814-5819 (2014).
- 20 Khan, A. I. *et al.* Negative capacitance in a ferroelectric capacitor. *Nat Mater* **14**, 182-186 (2015).
- 21 Luk'yanchuk, I. A., Lahoche, L. & Sene, A. Universal Properties of Ferroelectric Domains. *Phys Rev Lett* **102**, 147601 (2009).
- 22 Kopal, A., Mokry, P., Fousek, J. & Bahník, T. Displacements of 180 degrees domain walls in electroded ferroelectric single crystals: the effect of surface layers on restoring force. *Ferroelectrics* **223**, 127-134 (1999).
- 23 Dawber, M. *et al.* Tailoring the properties of artificially layered ferroelectric superlattices. *Adv Mater* **19**, 4153, (2007).
- 24 Wojdel, J. C., Hermet, P., Ljungberg, M. P., Ghosez, P. & Iniguez, J. First-principles model potentials for lattice-dynamical studies: general methodology and example of application to ferroic perovskite oxides. *J Phys-Condens Mat* **25**, 305401 (2013).
- 25 Blatter, G., Feigelman, M. V., Geshkenbein, V. B., Larkin, A. I. & Vinokur, V. M. Vortices in High-Temperature Superconductors. *Rev Mod Phys* **66**, 1125-1388 (1994).
- 26 De Guerville, F., Luk'yanchuk, I., Lahoche, L. & El Marssi, M. Modeling of ferroelectric domains in thin films and superlattices. *Mat Sci Eng B-Solid* **120**, 16-20 (2005).
- 27 Wojdel, J. C. & Iniguez, J. Ferroelectric Transitions at Ferroelectric Domain Walls Found from First Principles. *Phys Rev Lett* **112**, 247603 (2014).
- 28 Lichtensteiger, C., Fernandez-Pena, S., Weymann, C., Zubko, P. & Triscone, J.-M. Tuning of the Depolarization Field and Nanodomain Structure in Ferroelectric Thin Films. *Nano Lett* **14**, 4205-4211 (2014).
- 29 Aguado-Puente, P. & Junquera, J. Ferromagneticlike closure domains in ferroelectric ultrathin films: First-principles simulations. *Phys Rev Lett* **100**, 177601-, 177601 (2008).
- 30 Warusawithana, M. P. *et al.* A Ferroelectric Oxide Made Directly on Silicon. *Science* **324**, 367-370 (2009).

Acknowledgments: The authors gratefully acknowledge financial support from: EPSRC (Grant No. EP/M007073/1, P.Z. and M.H); the A. G. Leventis Foundation (M. H.); FNR Luxembourg (Grant No. FNR/P12/4853155/Kreisel, J. I.); MINECO-Spain (Grant No. MAT2013-40581-P, J.I. and J. C. W.); the Swiss National Science Foundation Division II (J.-M.T and S.F); the European Research Council under the European Union's Seventh Framework Programme (FP7/2007-2013)/ERC (Grant No. 319286 (Q-MAC), J.-M.T. and S.F); and the EU-FP7-ITN project NOTEDEV (Grant No. 607521. I.L.).

Main Figures

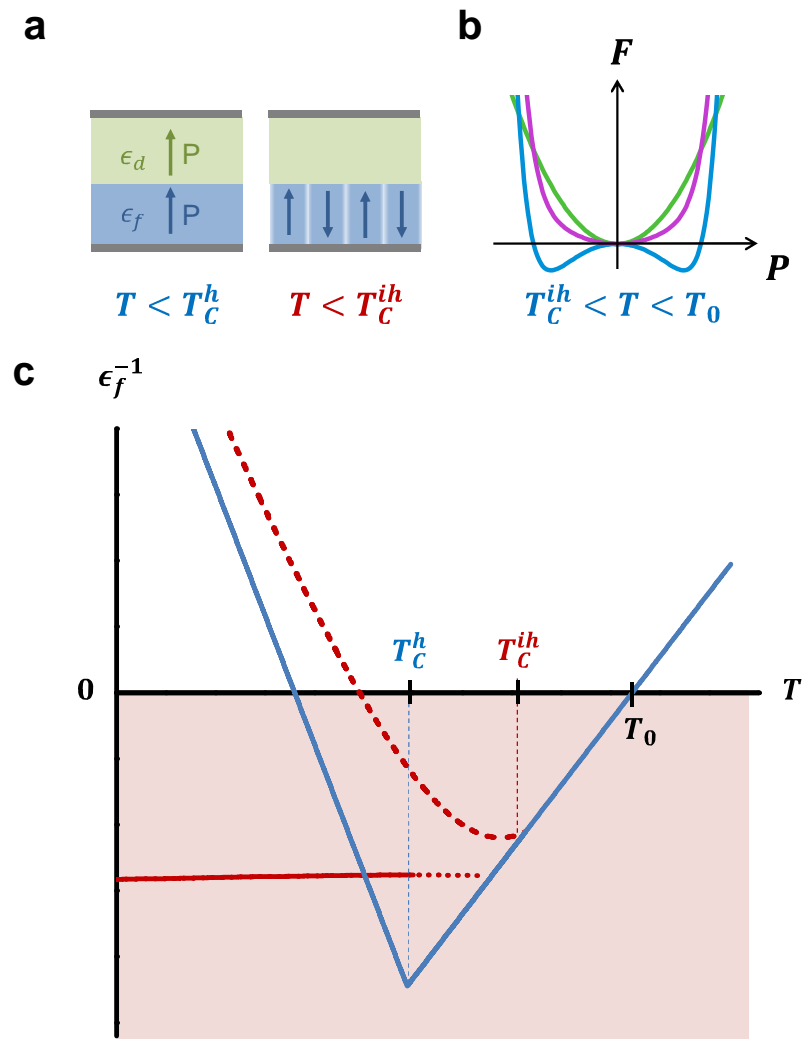


Figure 1 | Phenomenological description of negative capacitance. **a**, Sketch of the ferroelectric-dielectric bilayer capacitor with and without domains. Green, blue and grey layers correspond to the dielectric, ferroelectric and metallic components respectively. **b**, The total (purple) and local free energies of the ferroelectric (blue) and dielectric (green) layers. **c**, Temperature dependence of the local dielectric stiffness of the ferroelectric layer calculated from phenomenological models with: uniform homogeneous polarization (blue), and inhomogeneous polarization with static, soft domain walls (red, dashed) and mobile, abrupt domain walls (red, solid).

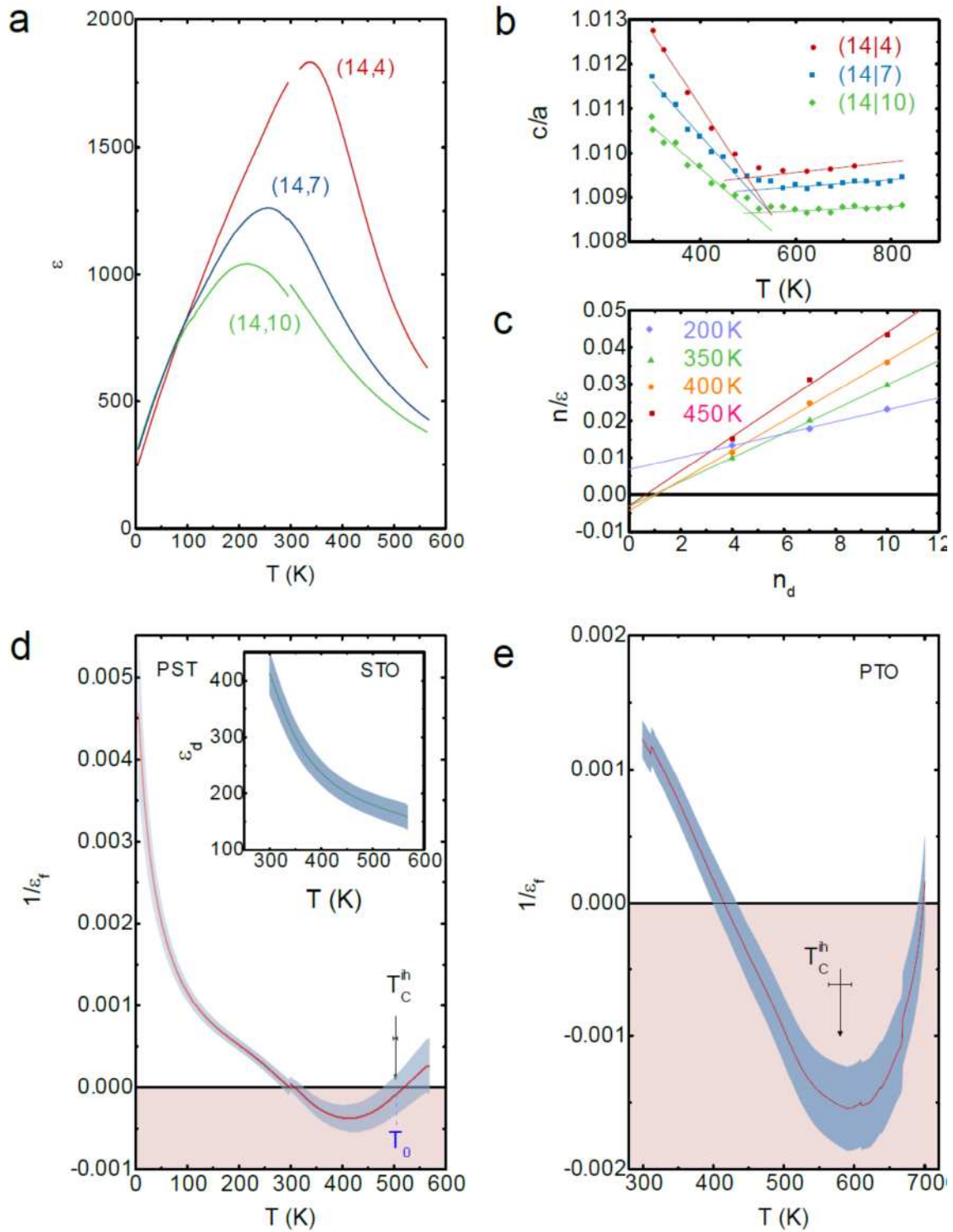


Figure 2 | Temperature dependence of the dielectric permittivities of PST-STO and PTO-STO superlattices. a, Total dielectric constant of $(14, n_d)$ PST-STO superlattices. **b**, Sample tetragonalities used to determine T_C . **c**, Linear fits to the series capacitor expression for a selection of temperatures. **d**, Reciprocal dielectric constant of the PST layers in $(14, n_d)$

superlattices calculated from the series capacitor model. Arrow with associated error bars indicates T_C . Inset shows the dielectric constant of the STO layers. Estimated uncertainties are shown as grey error bars. **e**, Reciprocal dielectric constant of the PTO layers in $(5, n_d)$ superlattices.

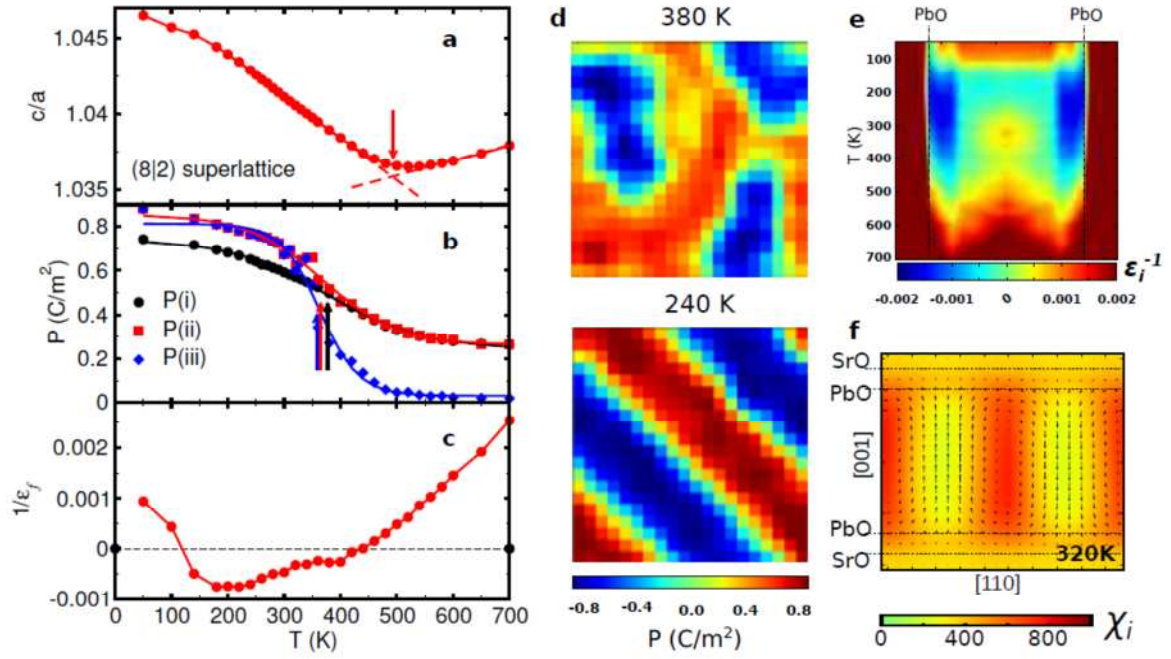


Figure 3 | Results of Monte Carlo simulations of a first-principles-based model for the (8,2) superlattice. Temperature dependence of the PTO layer **a**, c/a ratio; **b**, local polarisation; and **c**, reciprocal dielectric constant. **b**, Supercell average of the local polarisation absolute value (i), as well as the polarisation at a particular cell within a domain considering its absolute (ii) and bare (iii) values. The arrows mark the elastic transition and onset of fluctuating polar order around 490 K in **a** and the ferroelectric freezing transition around 370 K as determined from the inflection points in **b**. The high-temperature tails of P(i) and P(ii) reveal the presence of incipient polar order. **d**, Snapshots of the local polarisation (out-of-plane component) within the middle of the PTO layer at 380 K and 240 K. **e**, Temperature dependence of the local dielectric response $1/\epsilon_i$ resolved along the stacking direction. **f**, Local susceptibility map in the (-110) plane at 320 K.

Methods

Landau theory for monodomain bilayers and superlattices

To derive the expected temperature dependence of the dielectric function of a ferroelectric-dielectric bilayer or superlattice undergoing a phase transition to a homogenous (monodomain) state, we consider the free energy of the bilayer capacitor under short-circuit boundary conditions (or equivalently, one period of a superlattice) of the form

$$F = l_f \left(\frac{\alpha_f}{2} P^2 + \frac{\beta_f}{4} P^4 + \frac{\epsilon_0}{2} E_f^2 \right) + l_d \frac{\epsilon_0 \epsilon_d}{2} E_d^2. \quad (1)$$

The first term represents the energy density, per unit area, of a ferroelectric material with a second-order phase transition at a temperature T_0 as determined by the coefficient of the P^2 term, $\alpha_f = (T - T_0)/C\epsilon_0$. The second term describes the energy penalty for polarizing the dielectric layer with dielectric constant ϵ_d . Here E_f and E_d are the electric fields, appearing in the ferroelectric and dielectric layers respectively when the spontaneous polarisation P develops. Taking into account the electrostatic boundary conditions at the ferroelectric-dielectric interface $\epsilon_d \epsilon_0 E_d = \epsilon_0 E_f + P$ and the short-circuit condition for the whole system, $l_d E_d + l_f E_f = 0$, the functional (1) can be rewritten in terms of P only with a renormalized overall P^2 coefficient and the corresponding lowering of the transition temperature. The transition to a homogeneous ferroelectric state is thus predicted to occur at

$$T_C^h = T_0 - C \left(1 + \frac{l_f}{l_d} \epsilon_d \right)^{-1}$$

In particular, when $\epsilon_d \gg 1$ and l_d is comparable to l_f , (1) reduces to

$$F \approx l_f \left(\frac{\alpha_f}{2} P^2 + \frac{\beta_f}{4} P^4 \right) + l_d \left(\frac{1}{2\epsilon_0 \epsilon_d} P^2 \right)$$

which describes the energy of a homogeneously polarized bilayer with equal polarizations in both layers^{17,23}. T_C^h then simplifies to

$$T_C^h \approx T_0 - \frac{l_d}{l_f \epsilon_d} C.$$

The overall electric susceptibility of such a system is given by

$$\frac{l}{\chi} = \epsilon_0 \frac{\partial^2 F}{\partial P^2} = \frac{l_d}{\chi_d} + \frac{l_f}{\chi_f},$$

where $l = (l_f + l_d)$, and $\chi_d \approx \epsilon_d$ and $\chi_f = (\alpha_f + 3\beta_f P^2)^{-1} \epsilon_0^{-1}$ are the electric susceptibilities of the dielectric and ferroelectric layers respectively. It has the familiar form of the series capacitance formula $\frac{1}{C_{tot}} = \frac{1}{C_d} + \frac{1}{C_f}$. Note that for high permittivity materials, such as those considered in this work, $\chi = \epsilon$ to a very good approximation. The temperature dependence of the contribution to the reciprocal dielectric constant from the ferroelectric layer is shown in Fig 1c (blue curve). While the total permittivity exhibits the typical divergence ($\epsilon^{-1} = 0$) at T_C^h and is always positive, as required for thermodynamic stability, the dielectric stiffness of the ferroelectric component decreases linearly with temperature upon cooling and acquires negative values below T_0 . At T_C^h , the spontaneous polarisation appears and the $3\beta_f P^2$ term eventually restores ϵ_f^{-1} to positive values at lower temperatures. To obtain the blue curve in Fig. 1c, we have modelled a 30-nm-thick PbTiO₃ film in series with a 10-nm-thick SrTiO₃ layer using the following parameters: $T_0 = 1244$ K (strain-renormalized), $C = 4.1 \times 10^5$ K and $\epsilon_d = 300$, giving $T_C^h = 788$ K.

Landau-Kittel model of domain-wall contribution to permittivity

For an isolated ferroelectric slab of thickness l_f in zero applied field, the up- and down-oriented 180° domains are of equal width, w , given by the Landau-Kittel square-root dependence^{31,32}. For high- ϵ ferroelectrics

$$w \approx \left(\frac{\epsilon_{\perp}}{\epsilon_{\parallel}} \right)^{\frac{1}{4}} \sqrt{\zeta \cdot \lambda \cdot 2\xi \cdot l_f}$$

where ϵ_{\parallel} and ϵ_{\perp} are the ‘bulk’ lattice dielectric constants parallel and perpendicular to the polarization, ξ is the coherence length, $\lambda = 1 + \epsilon_d/(\epsilon_{\parallel} \epsilon_{\perp})^{1/2}$ and $\zeta \approx 3.53$ ^{5,12,26,33,34}. This equation also holds for ferroelectric films with dead layers and ferroelectric-dielectric superlattices, provided the dielectric layers are thick enough compared to the domain width to allow the interfacial stray fields to decay sufficiently. Upon application of a field, the ferroelectric layer develops a net polarization due to (i) the dielectric response of the lattice, described by ϵ_{\parallel} , and (ii) the motion of domain walls. To calculate the domain-wall contribution, one must find the field-induced changes to the stray depolarizing fields, as has been done in refs^{5,12,22}. The resulting effective dielectric constant of the ferroelectric can be expressed as¹²

$$\epsilon_f = \epsilon_{\parallel} - \frac{\pi}{4 \ln 2} \sqrt{\frac{\epsilon_{\perp}}{\epsilon_{\parallel}}} \frac{l_f}{w} \lambda \epsilon_{\parallel}$$

where the first term is the lattice response, while the second term is the *negative* contribution from domain-wall motion. Within the limits of validity of the Landau-Kittel theory l_f/w is large and therefore the second term is dominant. We stress again that this term originates from the field-induced changes in the inhomogeneous electric field distribution at the interface between the ferroelectric and the dielectric (or ‘dead’) layers, consistent with the findings of our atomistic calculations.

The temperature dependence of w and ϵ_f , can be estimated³⁵ using the standard critical Ginzburg-Landau expansions near T_0

$$\xi(T) = \frac{\xi_0}{(1 - T/T_0)^{1/2}}; \quad \epsilon_{\parallel}(T) = \frac{1}{2} \frac{\kappa_{\parallel}}{1 - T/T_0} \quad (3)$$

where κ_{\parallel} is related to the Curie constant C via $\kappa_{\parallel} = C/T_0$ and ξ_0 is the atomic-scale coherence length at $T = 0$. Assuming that ϵ_{\perp} is temperature independent, the domain width w is almost temperature independent^{21,26} whereas the approximate temperature dependence of ϵ_f is sketched in Fig. 1c. The solid red curve was calculated for a 30-nm-thick film with the following parameters (corresponding roughly to those of strained PbTiO₃): $T_0 = 1244$ K, $C = 4.1 \times 10^5$ K, $\epsilon_{\perp} = 120$ and $2\xi_0 = 1$ nm.

Ginzburg-Landau theory of polydomain bilayers and superlattices

The critical temperature of transition to the inhomogeneous striped domain state can be calculated within Ginzburg-Landau theory^{26,33},

$$T_C^{ih} = (1 - \pi\tau)T_0,$$

where $\tau = (C/T_0\epsilon_{\perp})^{\frac{1}{2}} \cdot 2\xi_0/l_f$. For 30nm-thick PTO film, we obtain $T_C^{ih} \simeq 1030$ K. A similar expression (up to a numerical factor) can be obtained on the qualitative level by noting that at T_C^{ih} the domain width w becomes comparable with the domain wall thickness $2\xi(T)$.

Close to T_C^{ih} , the Landau-Kittel thin-wall approximation breaks down as the domain profile becomes soft (we represent this region by the dotted line in Fig. 1c). The theory for mobile domain walls in this regime is challenging, but the lattice part of the response of the polydomain structure can be calculated analytically. This would correspond to a situation where domain wall motion is impeded, for instance by pinning of the domain walls. Using Ginzburg-Landau theory, this contribution can be expressed as³⁵

$$\epsilon_f(T) = \frac{2\epsilon_{\parallel}(T)}{3\langle P^2 \rangle / P_B^2 - 1}$$

which is a generalization of (3). Here $P_B = P_0 \left(1 - \frac{T}{T_0}\right)^{1/2}$ is the normalized temperature-dependent polarisation of the bulk short-circuited sample, and $\langle P^2 \rangle = \langle P^2(x, y) \rangle$ is the space

average of the temperature-dependent polarisation profile of the domain state with critical temperature T_C^{ih} . The factor $\langle P^2 \rangle$ can be calculated over a wide temperature interval that includes both soft and abrupt (thin) domain profiles using the universal expression for $P(x, y)$ in terms of elliptic sn -functions, as given in Eqn. (7) of ref. 21. After space-averaging we obtain

$$\epsilon_{f, GL}^{-1}(T) = \frac{T_0}{C} \left(\frac{T}{T_0} - 1 \right) \left[1 - 3F \left(1 - \frac{T}{T_C^{ih}} \right) \right], \quad T < T_C^{ih}$$

where $F(x) = \frac{1}{m^2} [K(m(x)) - E(m(x))]^2 \tanh(0.35\tau x)$; $K(m)$ and $E(m)$ are the complete elliptic integrals of the first and second kind respectively with $m(x) \approx \tanh 0.27\tau x$ and $\tau = (C/T_0\epsilon_{\perp})^{\frac{1}{2}} \cdot 2\xi_0/l_f$. Note that $F(0) = 0$ and the above expression matches the relative permittivity of the paraelectric state $\epsilon_p(T) = C/(T - T_0)$ at $T = T_C^{ih}$. The temperature dependence of $\epsilon_{f, GL}^{-1}$ is shown by the dashed red line in Fig. 1c.

Sample preparation

Superlattices were deposited on monocrystalline (100)-SrTiO₃ (STO) substrates using off-axis radiofrequency magnetron sputtering. PTO and STO were deposited at a substrate temperature of 520⁰C in an O₂/Ar mixture of ratio 5/7 and total pressure of 180 mTorr. For SRO layers, acting as top and bottom electrodes, the corresponding parameters were 635 ⁰C, 1/20 and 100 mTorr. PST layers were deposited by sequential sputtering of sub-monolayer amounts of STO and PTO. The PST-STO superlattices were asymmetrically terminated with bottom SRO-PST and top STO-SRO interfaces. By contrast, the PTO-STO superlattices were symmetrically terminated with both metal-insulator interfaces being between STO and SRO; the thickness of interfacial STO layers was chosen to be half of those in the superlattice interior to maintain a constant overall composition. For each series of superlattices, the thickness of the ferroelectric layers was fixed (14 unit cells (u.c.) for PST and 5 u.c. for PTO)

while the STO layer thickness was varied from 4 u.c. to 10 u.c. The number of repetitions N was chosen to maintain the total superlattice thickness as close as possible to 100 nm for PTO-STO superlattices and 200 nm for PST-STO superlattices. To extract the interface capacitance contribution, a series of $(5,8)_N$ PTO-STO superlattices with $N = 10, 19$ and 30 was used.

The top SRO layers were patterned using UV photolithography and etched using an Ar ion beam to form a series of $240 \times 240 \mu\text{m}^2$ capacitors. Structural characterization was performed using a PANalytical X'Pert PRO diffractometer equipped with a triple axis detector and an Anton Paar domed heating stage. Dielectric impedance spectroscopy in the 100 Hz to 2 MHz frequency range was performed using an Agilent E4980A Precision LCR meter in a tube furnace with a custom made sample holder under continuous O_2 flow at atmospheric pressure.

Structural analysis

Specular θ - 2θ scans were used to determine the superlattice periodicity (Extended Data Fig. 1a), whereas rocking curves were used to confirm the presence of domains and determine their periodicity (Extended Data Figs 1b and 1c). Temperature evolution of the lattice parameters was obtained from θ - 2θ scans and used to determine the phase transition temperatures, taken to be the crossing point of linear fits to the high and low temperature data (see Fig 2b).

Calculation of the individual layer permittivities

The total measured capacitance of the sample C_{tot} has contributions from the superlattice C_{SL} and the two metal-dielectric interfaces C_i

$$\frac{1}{C_{tot}} = \frac{1}{C_{SL}} + \frac{2}{C_i} = \frac{1}{C_f} + \frac{1}{C_d} + \frac{2}{C_i}$$

where C_f and C_d are the total (series) capacitance of all the ferroelectric (PTO) and dielectric (STO) layers respectively. For an $(n_f, n_d)_N$ superlattice

$$\frac{d}{\epsilon} = \frac{d_d}{\epsilon_d} + \frac{d_f}{\epsilon_f} + \frac{2}{\tilde{C}_i}$$

$$\frac{N(n_f + n_d) \bar{c}}{\epsilon} = \frac{Nn_d c_d}{\epsilon_d} + \frac{Nn_f c_f}{\epsilon_f} + \frac{2}{\tilde{C}_i}$$

where $\tilde{C}_i = C_i/\epsilon_0 A$, d_j are the relevant thicknesses and c_j are the lattice constants. Since $c_f \approx c_d \approx \bar{c} = (n_d c_d + n_f c_f)/(n_d + n_f)$

$$\frac{n_d + n_f}{\epsilon} \equiv \frac{n}{\epsilon} \approx \frac{n_d}{\epsilon_d} + \frac{n_f}{\epsilon_f} + \frac{2}{N\bar{c}\tilde{C}_i}$$

For a series of superlattices with a fixed period (i.e. fixed n_f and n_d) but varying N the interfacial contribution $1/(\bar{c}\tilde{C}_i)$ can be obtained from the slope of a plot of n/ϵ vs $1/N$.

Once the temperature dependence of the interfacial capacitance is known, the individual layer permittivities of the STO and PTO layers can be obtained using a series of samples with fixed n_f and varying n_d from the slope and intercept of the plot of $n/\epsilon - 2/(N\bar{c}\tilde{C}_i)$ vs n_d .

This analysis relies on the assumption that the layer permittivities do not change as the individual layer thicknesses are varied within each superlattice series. It is therefore crucial that the ferroelectric layer thickness is held fixed as it determines the periodicity of the ferroelectric domain structure and thus the ferroelectric transition temperature and the domain-wall contribution to the measured dielectric constant. All superlattices within a series must also be in the same regime of electrostatic coupling, which places a lower limit on the STO layer thickness at around 3-4 unit cells³⁶.

To quantify the interface contribution C_i for the PTO-based superlattices, a series of symmetrically terminated samples with a fixed period $(5,8)_N$ but varying number of

repetitions N was fabricated. The interface capacitance was extracted from the intercept of the plot of n/ϵ vs $1/N$ as discussed above and is shown as a function of temperature in Extended Data Fig. 4. At room temperature, C_i is around $1000 \text{ fF}/\mu\text{m}^2$, which is in excellent agreement with previous experimental work³⁷ and compares quite well with the DFT prediction of $615 \text{ fF}/\mu\text{m}^2$ (at 0 K) for the same interface³⁸. The weak dependence of C_i on temperature is also consistent with previous reports³⁷. Quantifying the interfacial contribution independently in this way allows us to extract more reliably the temperature range of the NC regime. As illustrated in Extended Data Fig. 4, the interfacial contribution does not change the qualitative behaviour of the extracted PTO dielectric constant and makes only a small (within error bars) difference to the extracted PTO stiffness. It is thus reasonable to neglect this correction, as was done in Fig. 2.

Impedance analysis

The observation of NC relies on the electrostatic interactions between the ferroelectric and dielectric layers, which in turn require both materials to be sufficiently insulating to avoid the screening of the spontaneous polarization. To identify the origin of dielectric losses and quantify the conductivity of our samples we have measured complex impedance spectra over a wide range of frequencies from 100 Hz to 2 MHz and performed equivalent circuit modelling. We present the complex impedance $Z(\omega) = Z' + iZ''$ data in the complex capacitance representation $C(\omega) = C' + iC'' \equiv 1/i\omega Z(\omega)$ as is common for capacitive systems.

Each PTO and STO layer in the superlattice, as well as the two metal-dielectric interfaces, can be considered as a parallel R-C element, with a capacitance C_j and a resistance R_j due to the finite conductivity of the layer. The superlattice is then modeled by connecting these R-C elements in series as shown in the inset of Extended Data Fig. 5. An additional series

resistance R_s (typically a few hundred Ω) accounts for the contact resistances and other sources of resistance in the external circuit.

At low temperature, the conductivities of the PTO and STO layers are negligible and the whole system behaves as a single capacitance $C = (\sum_j C_j^{-1})^{-1}$. The measured C' is frequency independent except for the high-frequency roll off due to the parasitic series resistance R_s . As shown in Extended Data Fig. 5 for a (5,8)₃₀ PTO-STO superlattice, even at 500 K, the data can be well modelled by a single capacitor in series with R_s ; the parallel resistance is too high to be determined from the fit (i.e. well above $10^8 \Omega$). At higher temperatures, the superlattice conductivity increases resulting in an increase of the dielectric loss C'' at low frequencies. The 600 K data are modelled with one parallel R-C element in series with R_s . Despite the high temperature and large electrode area ($240 \mu\text{m} \times 240 \mu\text{m}$), total sample resistance is still 2 M Ω . At 700 K, however, the total sample resistance drops to 8.8 k Ω . In addition, some layers become significantly more conducting than others, giving rise to Maxwell-Wagner relaxations³⁹ which can be observed as steps and plateaus in $C'(\omega)$. The behaviour can be qualitatively captured by dividing the system into two blocks with different resistances, each modelled as a parallel R-C element. To reproduce the more gradual frequency dispersion, however, more R-C elements are needed (in this case three were sufficient). At these temperatures, the samples are too conducting to maintain the electrostatic conditions necessary for NC. The sample resistances for all data shown in Fig. 2 were higher than 1 M Ω .

Atomistic simulations of PbTiO₃/SrTiO₃ superlattices

To construct the first-principles models for the PTO/STO superlattices, we took advantage of the potentials for the bulk compounds recently introduced by some of us,²⁴ which give a qualitatively correct description of the lattice-dynamical properties and structural phase transitions of both materials. Then, we treated the interface between PTO and STO in an

approximate way, relying on the following observations: (1) The inter-atomic force constants in perovskite oxides like PTO and STO have been shown to depend strongly on the identity of the involved chemical species and weakly on the chemical environment⁴⁰. (Thus, for example, the interactions between Ti and O are very similar in both PTO and STO.) (2) Except in the limit of very short-period superlattices, the main effects of the stacking are purely electrostatic and largely independent of the details of the interactions at the interfaces. (3) The main purely-interfacial effects leading, e.g., to the occurrence of new orders (as those discussed in ref. ⁴¹) are related to the symmetry breaking, which permits new couplings forbidden by symmetry in the bulk case. Such qualitative symmetry-breaking effects are trivially captured by our potentials, even if the actual values of the interactions are approximate. (Similar approaches to treat ferroelectric superlattices and junctions can be found in the literature, ref. 42 being a representative case.)

As a result of these approximations, we were able to construct our superlattice potentials by using the models for bulk PTO and STO to describe the interactions within the layers, assuming a simple numerical average for the interactions of the ion pairs touching or crossing the interface. Thus, for example, Ti—O interactions in a TiO₂ interface plane are computed as the average of the analogous Ti—O interactions in PTO and STO. New interactions, such as those involving Pb and Sr neighbours across the interface, are chosen so that the acoustic sum rules are respected; in practice, their values are close to an average between the analogous Sr—Sr and Pb—Pb pairs. Finally, the long-range dipole-dipole interactions are governed by a bare electronic dielectric constant ϵ_∞ that is taken as a weighted average of the first-principles results for bulk PTO ($8.5\epsilon_0$) and STO ($6.2\epsilon_0$), with weights reflecting the composition of the superlattice.

The parameters of our models for bulk PTO and STO were computed from first principles as described in ref. 24. To model our PTO/STO superlattices, we adjusted our models in the

following ways: (1) We softened the model for bulk STO so that it has a dielectric permittivity ϵ_{33} of about $300\epsilon_0$ at room temperature. We checked a posteriori that the STO layers in the superlattices are not as soft, which is probably a consequence of the modified electrostatic interactions (ϵ_∞) assumed, as described above. (2) We imposed an epitaxial constraint corresponding to having a STO (001)-oriented substrate, i.e., we assume in-plane lattice constants $a = b = 3.901 \text{ \AA}$, forming an angle $\gamma = 90^\circ$. (3) We tweaked the model for PTO so that it gives an out-of-plane polarization of 1.0 C/m^2 at 0 K when subject to the epitaxial constraint just described. Care was needed as the model of ref. 24 for bulk PTO becomes unstable when the epitaxial constraint is used in combination with the change in ϵ_∞ . Nevertheless, it was possible to obtain a stable model with the correct ground state polarisation by adjusting the expansive hydrostatic pressure introduced in ref. 24 as an empirical correction: instead of the -13.9 GPa used in ref. 24, for the present work we used -11.2 GPa . Note also that, when we use this model to simulate a film of PTO under the STO epitaxial constraint, we get a ferroelectric transition temperature of 460 K , which is slightly below the temperature at which the fluctuating domains appear in the (8,2) superlattice (490 K). As in the case of STO, the difference between bulk material and superlattice is probably caused by the different value of ϵ_∞ : we use a slightly larger value for the pure film, which results in a weaker ferroelectric instability.

These approximations and adjustments allow us to construct models for superlattices of arbitrary (n_f, n_d) stacking. For the simulations we used periodically-repeated supercells that contain 10×10 elemental perovskite units in-plane, while out-of-plane they expand one full superlattice period. Thus, for example, for the (8,2) superlattice we used a simulation box that contains $10 \times 10 \times (8+2) \times 5 = 5000$ atoms. We solved the models by running Monte Carlo simulations comprising between 10000 and 40000 thermalization sweeps (longer thermalization is needed in the vicinity of phase transitions) followed by 50000 sweeps to

compute thermal averages. The dielectric susceptibility was calculated by applying a small out-of-plane electric field to the simulation box. We found that, in this highly reactive system, this approach converged much faster than the usual fluctuation formulas⁴³.

The low-temperature ground state of our (8,2) superlattice is sketched in Extended Data Fig. 2, where the stripe domain structure can be nicely appreciated. Note that this result closely resembles the one obtained directly from first principles calculations, in the limit of 0 K, in ref. 44; this agreement further confirms the accuracy of our model potential.

Calculation of local dielectric constants

In the following we summarize the derivation of formulas that relate the local response of each layer with the global one of the superlattice. Here we are exclusively concerned with the response along the superlattice stacking direction. We use a “0” superscript to refer to the situation in which no external electric field is applied, and i to label the layers in the superlattice. In absence of free charges, the condition on the continuity of the displacement vector implies

$$D_i^0 = D^0 = P_i^0 + \epsilon_0 E_i^0$$

for all layers. Note that E_i^0 is the total electric field acting on layer i . In general, this total field can be split into local and external contributions, so that $E_i = E_{i,loc} + E_{ext}$. Naturally, when no external field is applied, we simply have $E_i^0 = E_{i,loc}^0$.

Additionally, if we have M layers in the repeated unit of the superlattice, the periodicity of the potential implies that

$$\sum_{i=1}^M l_i E_i^0 = 0,$$

where l_i is the thickness of layer i . Hence, in absence of applied field, there is no net potential drop across the supercell. Then, we immediately get that

$$D^0 = L^{-1} \sum_{i=1}^M l_i D_i^0 = L^{-1} \sum_{i=1}^M l_i P_i^0 = P^0,$$

Where $L = \sum_{i=1}^M l_i$ is one superlattice period and P^0 is the polarisation of the superlattice with no field applied. As a result, the electric field at layer i can be written as:

$$E_i^0 = E_{i,loc}^0 = (P^0 - P_i^0)/\epsilon_0.$$

Now we consider an external electric field E_{ext} . It is trivial to verify that the field-induced variations in polarisation, electric field and displacement satisfy:

$$\Delta D_i = \Delta D = \Delta P_i + \epsilon_0 (\Delta E_{i,loc} + E_{ext}) = \Delta P + \epsilon \epsilon_0 E_{ext},$$

$$\sum_{i=1}^M l_i \Delta E_{i,loc} = 0$$

and

$$\Delta E_{i,loc} = (\Delta P - \Delta P_i)/\epsilon_0.$$

Then, the dielectric constant of layer i can be computed as:

$$\epsilon_i = \frac{\Delta D}{\epsilon_0 \Delta E_i} = \frac{(\Delta P + \epsilon_0 E_{ext})}{\Delta P - \Delta P_i + \epsilon_0 E_{ext}} = \frac{(\chi + 1)}{\chi - \chi_i + 1} = \frac{\epsilon_{tot}}{\epsilon_{tot} - \chi_i},$$

where we have introduced the layer susceptibility

$$\chi_i = \frac{1}{\epsilon_0} \frac{\Delta P_i}{E_{ext}}.$$

As a result, we have managed to write all the relevant quantities in terms of the local susceptibilities χ_i , which is very convenient at both conceptual and practical levels.

Conceptually, χ_i is a quantity we expect to be positive in all cases, as an applied electric field

will create dipoles parallel to it. This basic local response of the material is physically and intuitively clear, as it is free from the subtleties (associated to the long-range electrostatic effects encapsulated in the local – depolarizing – fields) that affect the dielectric constant. Practically, χ_i is very easy to compute from a Monte Carlo simulation, may it be by explicitly applying an electric field and calculating the change in local polarisation *or* by directly inspecting the fluctuations of the local polarisations in absence of applied field. The latter approach can be viewed as a generalisation of the method described e.g. in ref. ⁴³; similar fluctuation formulas for ferroelectric nanostructures were introduced in refs ^{13,45}.

The layers labeled by i will typically correspond to actual PTO and STO layers, but we could also further sub-divide our superlattice. For example, the above formulas formally allow us to consider contributions from the interfaces, or from different regions within a layer. This kind of subdivision was used in our paper to prepare Fig. 3e, where maps of the dielectric constant as a function of position along the superlattice stacking direction are reported.

The dielectric susceptibility χ_i of a layer i can be viewed as a direct average of the susceptibilities $\chi_i(x, y)$ coming from different regions of the layer xy plane. Hence, we can use a representation as that of Fig. 3f in our manuscript to determine which part of a given layer (domain walls vs. domains) contributes the most to χ_i . Note that one could feel tempted to interpret the layer dielectric constant ϵ_i as coming from a collection of parallel capacitors, which would formally allow us to map $\epsilon_i(x, y)$. Such a construction, however, implicitly assumes an equal potential drop across the individual capacitors within layer i , which seems in conflict with the inhomogeneous in-plane structure of our PTO layers.

For the calculation of local polarizations, we evaluated the local dipole and cell volume from the atomic positions and Born effective charges. We computed dipoles centred on the A (Pb/Sr) and B (Ti) sites of the perovskite structure, by considering the weighted contributions of the surrounding atoms. Thus, for example, the dipole centred on a specific Ti cation was

computed by adding up contributions from the Ti itself, the 6 neighbouring oxygens (each such contribution was divided by 2, as each oxygen has 2 first-neighbour Ti cations) and the 8 neighbouring A (Pb/Sr) cations (each such contribution was divided by 8, as each A-cation has 8 first-neighbour Ti's).

Relation between atomistic simulations and experiment

As already mentioned, our model potentials for PTO/STO superlattices are not expected to render quantitatively accurate results. The difficulties to reproduce the behaviour of the bulk compounds in a quantitative way are discussed at some length in refs 24 and 46, where evidence is given of the great challenge these materials pose to first-principles methods. The model deficiencies are best captured by the error in the obtained transition temperatures: the model for PTO used in this work gives a value of 440 K when solved in bulk-like conditions, far below the experimental result of 760 K. Similarly, we do not expect our models to capture accurately the dielectric response of the STO layers in the superlattice, which we have checked tend to be stiffer than the experimental ones. Fortunately, beyond these quantitative inaccuracies, the qualitative behaviour of individual PTO and STO obtained from our simulations, as well as that of the PTO/STO superlattice, seem perfectly in line with experimental observations and physical soundness.

As regards the results for the PTO/STO system, it is interesting to note that our atomistic simulations predict a phase transition occurring in two steps: At a relatively high temperature (490 K) the c/a ratio of the PTO layers clearly reflects the onset of local instantaneous ferroelectric order; then, at a lower temperature (~ 370 K), the static multi-domain ferroelectric state freezes in. Thus, according to these simulations, the interval between 370 K and 490 K is characterised by strongly fluctuating ferroelectric domains. Admittedly, this result is likely to be affected by finite-size effects in our simulations; yet, given the very large separation of the two transition temperatures, and the easy and frequent domain

rearrangements observed in our Monte Carlo simulations, we tend to believe it should be taken seriously. Experimentally, preliminary measurements on the $(5,4)_{28}$ PTO-STO superlattice (Extended Data Fig. 6) indicate that the kink in the measured temperature dependence of the c/a ratio (usually assumed to mark the ferroelectric transition) occurs at a slightly (~ 50 K) higher temperature than the appearance of domain satellites in the diffuse scattering. A similar temperature difference was noted in a superlattice of a different composition in Fig. 3 of ref. 47. Further investigation is needed, however, to clarify the polarisation structure in this temperature range.

We also ran simulations of various $(8, n_d)$ superlattices, and computed the corresponding total dielectric constants as a function of temperature, to mimic our experimental approach to estimate the response of the PTO layer. Extended Data Fig. 3 shows the results for ϵ_f obtained in this way: reassuringly, we find a temperature interval where the PTO layers present a negative dielectric constant, which validates our experimental strategy for estimating ϵ_f .

If we compare the results in Extended Data Fig.3 and Fig. 3c of our manuscript, we note that the temperature interval in which the negative capacitance is observed is essentially the same, but the quantitative values for ϵ_f clearly differ. Nevertheless, given the approximations involved in each of the two methods to compute ϵ_f – e.g., heuristic division into PTO and STO layers, implicit assumption that PTO layers in $(8, n_d)$ superlattices of varying STO content behave equivalently, etc. – these quantitative discrepancies do not seem very significant and we have not investigated them further.

Finally, returning to our phenomenological predictions in Fig. 1c, it would appear that the Landau-Ginzburg result for the static domain structure bears a closer qualitative resemblance to the experimental data and the atomistic simulation results than the Kittel model, despite the

fact that it is the latter which correctly captures the important contribution of domain wall motion. It is important to note, however, that in the Kittel model above we have not included the possibility of domain wall pinning (by defects or otherwise), which would reduce the domain wall contribution and could lead to an upturn of ϵ_f at low temperatures. Quantifying the relative contributions to NC from domain wall motion and the static domain response, both experimentally and through atomistic simulations, would be a worthwhile challenge for future studies.

Supplementary Information is linked to the online version of the paper at www.nature.com/nature.

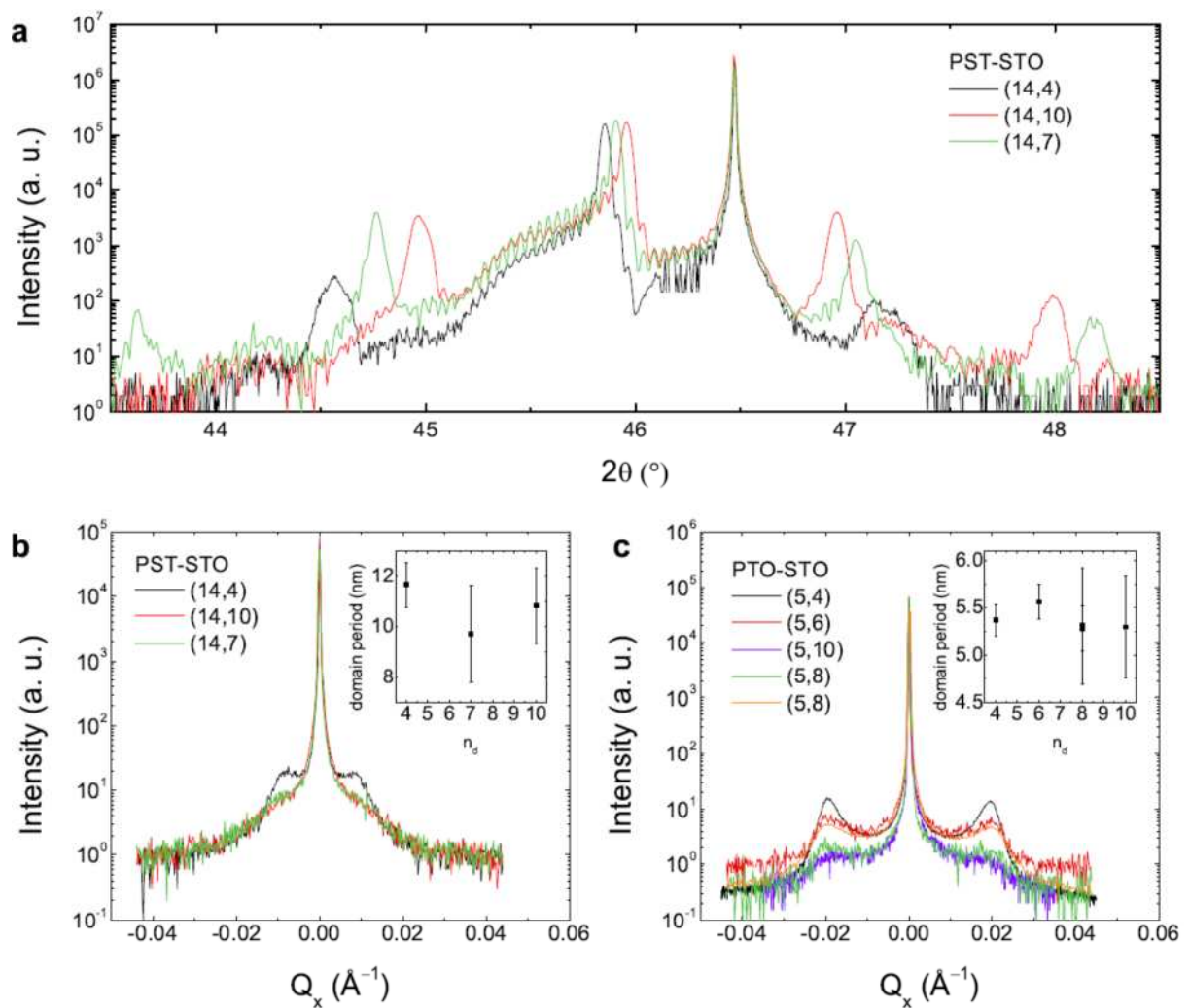
Author contributions

P.Z., M.H., S.F. and J.-M.T. performed and analysed the experiments. A.S. and I.L. developed the phenomenological theory. J.C.W. and J.I. developed the atomistic models and performed the simulations.

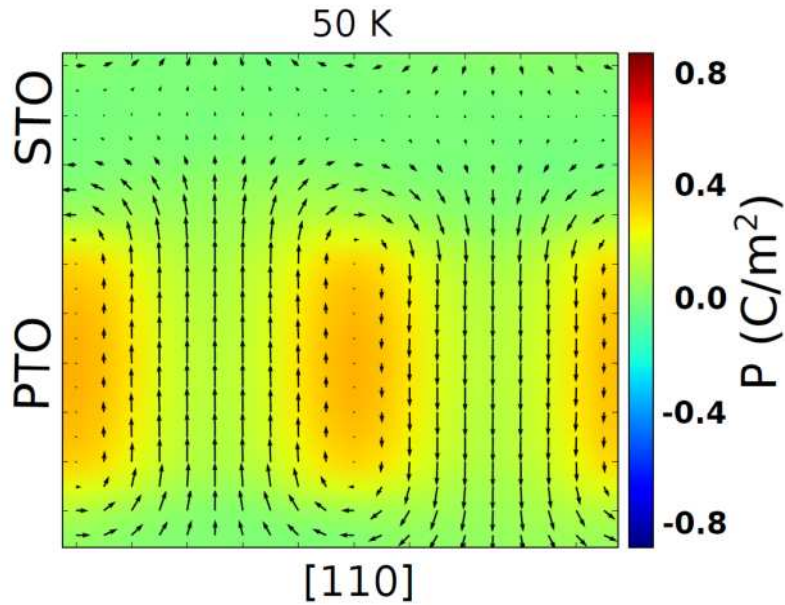
Author information

Reprints and permissions information is available at www.nature.com/reprints. The authors declare no competing financial interests. Correspondence and requests for materials should be addressed to P.Z. (p.zubko@ucl.ac.uk) and J.I. (jorge.iniguez@list.lu).

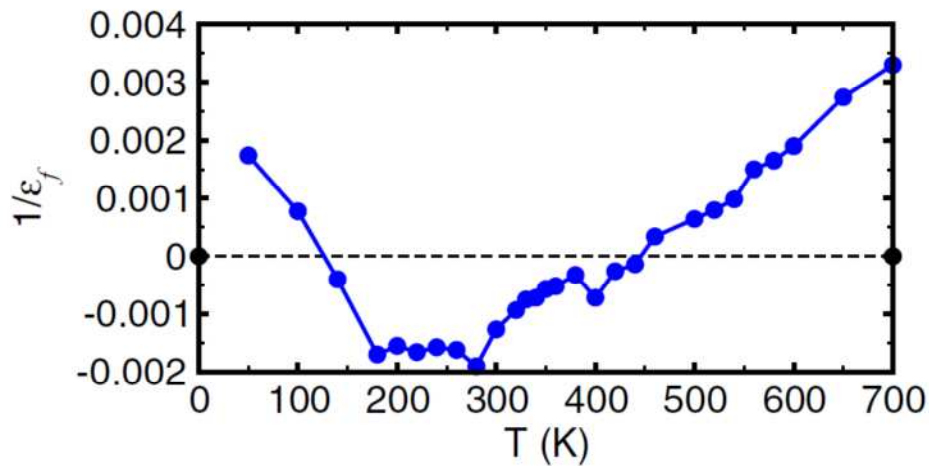
Extended Data



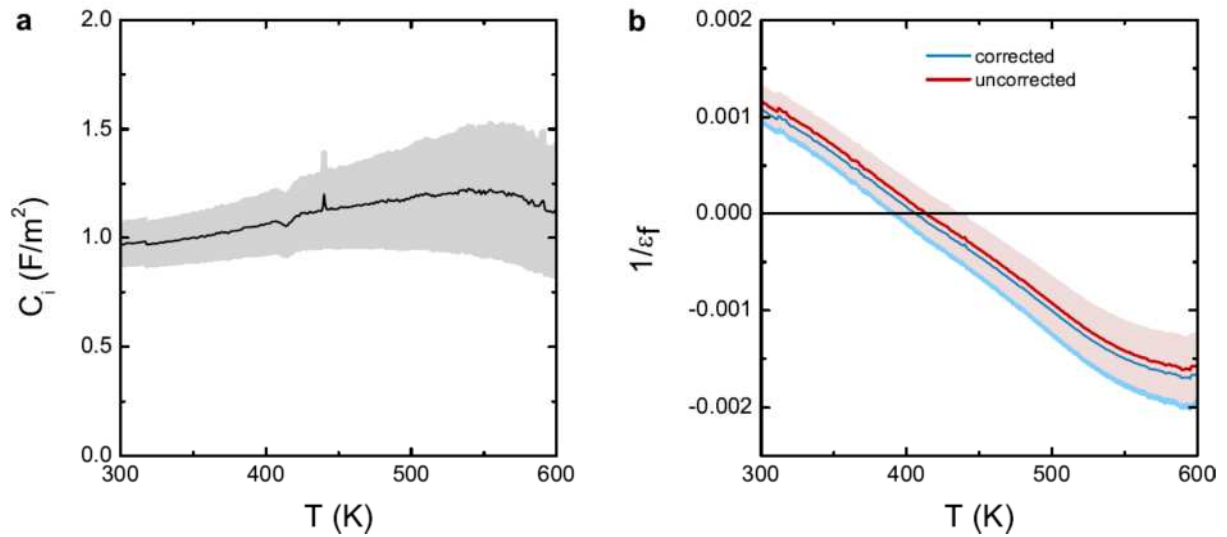
Extended Data Figure 1 | XRD characterisation of the superlattices. **a**, Intensity profiles around the (002) substrate reflection for PST-STO superlattices. The broad peaks around $2\theta = 45.5^\circ$ correspond to the top and bottom SRO electrodes. Finite size oscillations due to the 200 nm superlattice thickness are visible. **a** and **b**, XRD domain satellites for **a**, PST-STO and **b**, PTO-STO superlattices. Insets: domain periodicities obtained from fitting the Q_x line profiles using a sum of two Gaussian and one Lorentzian functions for the domain satellites and central Bragg peak respectively.



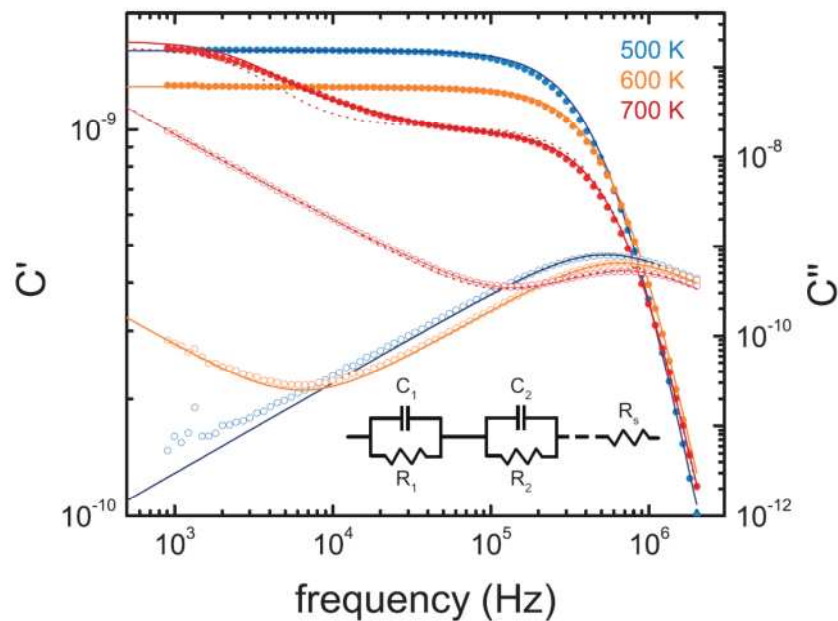
Extended Data Figure 2 | Local polarization distribution at low temperature. Arrows indicate the dipole component within the (-110) plane; we plot arrows for both Pb/Sr-centred and Ti-centred dipoles. The colouring indicates the polarisation component along $[-110]$, revealing a low-temperature polar order at the domain walls.



Extended Data Figure 3 | Comparison with experiment. Reciprocal dielectric constant of the PTO layers calculated from the computed total dielectric constants of $(8, n_d)$ superlattices using the same analysis as for the experimental data.



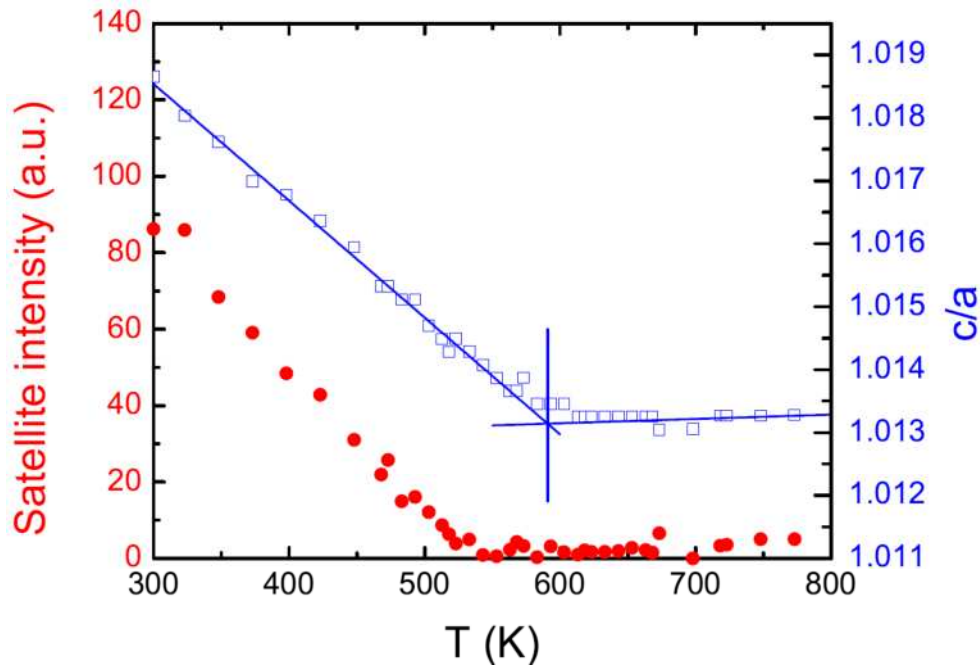
Extended Data Figure 4 | Interface capacitance contributions. **a**, SRO-STO interface contribution to the dielectric response. **b**, Dielectric stiffness of the PTO layers with and without correcting for the interface capacitance.



Extended Data Figure 5 | Dielectric impedance spectroscopy of PTO-STO superlattices.

Real (full circles) and imaginary (open circles) parts of the complex capacitance function $C = C' + iC''$ for a $(5,8)_{30}$ PTO-STO superlattice. For temperatures below ~ 650 K, the data can be well fitted with a single parallel R-C element in series with R_s , as shown by solid curves for the 500 K and 600 K data. At higher temperatures, Maxwell-Wagner relaxations

appear as the conductivities of some layers increase faster with temperature than others. At 700 K, the response can be qualitatively captured by a model with two parallel R-C elements in series with each other (dashed red curve), while for a quantitative fit three R-C elements are required (solid red curve).



Extended Data Figure 6 | Temperature evolution of the tetragonality and domain satellites. Intensity of the XRD domain satellite (red) and the film tetragonality (blue) for a $(5,4)_{28}$ PTO-STO superlattice. The satellite intensity was obtained by integrating the measured intensity of the domain satellites and subtracting the minimum integrated intensity in the paraelectric phase.

Supplementary Video | High temperature fluctuations of the domain structure. Local dipoles (z component) at the mid plane of the PbTiO_3 layer in our (8,2) simulated superlattice. The video is constructed from snapshots of a Monte Carlo simulation at 400 K.

References

- 31 Landau, L. D. & Lifshitz, E. M. Theory of the dispersion of magnetic permeability in ferromagnetic bodies. *Phys. Z. Sowjetunion* 8, 153 (1935).
- 32 Kittel, C. Theory of the Structure of Ferromagnetic Domains in Films and Small Particles. *Phys Rev* 70, 965-971 (1946).
- 33 Stephanovich, V. A., Luk'yanchuk, I. A. & Karkut, M. G. Domain-enhanced interlayer coupling in ferroelectric/paraelectric superlattices. *Phys Rev Lett* 94, 047601 (2005).
- 34 Catalan, G., Schilling, A., Scott, J. F. & Gregg, J. M. Domains in three-dimensional ferroelectric nanostructures: theory and experiment. *J Phys-Condens Mat* 19, 132201 (2007).
- 35 Sené, A. Theory of domains and nonuniform textures in ferroelectrics. *Ph.D. thesis, Universite de Picardie, France* (2010).
- 36 Zubko, P. *et al.* Electrostatic Coupling and Local Structural Distortions at Interfaces in Ferroelectric/Paraelectric Superlattices. *Nano Lett* 12, 2846-2851 (2012).
- 37 Plonka, R., Dittmann, R., Pertsev, N. A., Vasco, E. & Waser, R. Impact of the top-electrode material on the permittivity of single-crystalline Ba_{0.7}Sr_{0.3}TiO₃ thin films. *Appl Phys Lett* 86, 202908 (2005).
- 38 Stengel, M. & Spaldin, N. A. Origin of the dielectric dead layer in nanoscale capacitors. *Nature* 443, 679-682 (2006).
- 39 Catalan, G., O'Neill, D., Bowman, R. M. & Gregg, J. M. Relaxor features in ferroelectric superlattices: A Maxwell-Wagner approach. *Appl Phys Lett* 77, 3078-3080 (2000).
- 40 Ghosez, P., Cockayne, E., Waghmare, U. V. & Rabe, K. M. Lattice dynamics of BaTiO₃, PbTiO₃, and PbZrO₃: A comparative first-principles study. *Phys Rev B* 60, 836-843 (1999).
- 41 Bousquet, E. *et al.* Improper ferroelectricity in perovskite oxide artificial superlattices. *Nature* 452, 732-734 (2008).
- 42 Lisenkov, S. & Bellaiche, L. Phase diagrams of BaTiO₃/SrTiO₃ superlattices from first principles. *Phys Rev B* 76, 020102 (2007).
- 43 Garcia, A. & Vanderbilt, D. Electromechanical behavior of BaTiO₃ from first principles. *Appl Phys Lett* 72, 2981-2983 (1998).
- 44 Aguado-Puente, P. & Junquera, J. Structural and energetic properties of domains in PbTiO₃/SrTiO₃ superlattices from first principles. *Phys Rev B* 85, 184105 (2012).

- 45 Ponomareva, I., Bellaiche, L. & Resta, R. Relation between dielectric responses and polarization fluctuations in ferroelectric nanostructures. *Phys Rev B* 76, 235403 (2007).
- 46 Wojdel, J. C. & Iniguez, J. Testing simple predictors for the temperature of a structural phase transition. *Phys Rev B* 90, 014105 (2014).
- 47 Zubko, P. *et al.* Ferroelectric Domains in PbTiO₃/SrTiO₃ Superlattices. *Ferroelectrics* 433, 127-137 (2012).